RSC Advances

PAPER

Cite this: *RSC Adv.*, 2025, **15**, 9636

Amorphous/crystalline nanostructured Co–FeOOH/CoCe-MOF/NF heterojunctions for efficient electrocatalytic overall water splitting†

Chang Su,[ab] Dan Wang,[c] Wenchang Wang,[c] Naotoshi Mitsuzaki[d] and Zhidong Chen *[c]

Received 24th December 2024
Accepted 13th February 2025

DOI: 10.1039/d4ra08980d

rsc.li/rsc-advances

Hydrogen production by electrocatalytic water splitting is considered to be an effective and environmental method, and the design of an electrocatalyst with high efficiency, low cost, and multifunction is of great importance. Herein, we developed a amorphous Co–FeOOH/crystalline CoCe-MOF heterostructure (defined as Co–FeOOH/CoCe-MOF/NF) though a convenient cathodic electrodeposition strategy as a high-efficiency bifunctional electrocatalyst for water electrolysis. The Co–FeOOH/CoCe-MOF/NF nanocrystals provide remarkable electronic conductivity and plenty of active sites, and the crystalline/amorphous heterostructure with generates synergistic effects, providing plentiful active sites and efficient charge/mass transfer. Benefiting from this, the designed Co–FeOOH/CoCe-MOF/NF displays ultralow overpotentials of 226 and 74 mV to achieve 10 mA cm^{-2} for oxygen evolution reaction and hydrogen evolution reaction, and also shows the superior performance for overall water splitting with a low voltage of 1.55 V at 10 mA cm^{-2} in 1 M KOH. The work reveals a design of superior activity, cost-effective and multifunctional electrocatalysts for water splitting.

1. Introduction

Hydrogen is a widely recognized renewable and clean energy source, which is considered a reliable substitute for fossil fuels. Compared with the traditional production methods of catalytic reforming or dehydrogenation, electrochemical water splitting (EWS) is a more environmentally friendly and economic route to produce high purity hydrogen, especially using the electricity from renewable sources such as wind and solar or the traditional electricity during off-peak hours.[1–4] The technology and applications of EWS are mature and can be implemented on a large scale, but at high cost and with significant energy consumption.[5,6] Therefore, given the need for environmental protection and increasingly limited material resources, hydrogen production *via* water electrolysis is a key research direction. Electrolytic water can be divided into two half reactions: an anode generated OER, and a cathode generated HER, which are combined effectively and thus enhanced kinetics of water electrolysis.[7–10] Currently, Pt-based catalysts have shown the best performance for the HER, whereas RuO_x/IrO_x is the baseline catalyst for the OER.[11–14] However, the high cost and limited reserves of noble metals hinder their large-scale use.[15,16] Consequently, there is a crucial need to produce an economical and superior electrocatalyst, with effectiveness, and high stability.

Metal–organic frameworks (MOFs) are a family of crystalline porous materials, which have high specific surface area, tunable ordered structure and abundant intrinsic molecular metal sites, have been regarded as ideal catalyst candidates.[17–21] Despite the above advantages, there are some concerns when considering MOFs as catalysts. These may include a slow mass transfer, a low electrical conductivity, and a framework and structural instability during the electrocatalytic applications.[22–25] Besides, the MOF-derivates always show greatly improved conductivity and activity for OER and HER, but the intrinsic well-defined structure and channels are always collapsed during the post-treatment process.[26–28] Therefore, many efforts have been made to increase the conductivities of these materials without damaging the MOF structure. Recent studies have shown that synthesis of bimetallic or poly-metallic MOFs can be significantly improve the electrocatalytic performance for overall water splitting due to the synergistic effect between bimetallic atoms.[3,29–31] Among various bimetallic MOFs, CoCe bimetallic MOFs displayed state-of-the-art catalytic performance and the most extensive application prospect by virtue of high specific surface area, significant structural complexity and flexible characters. And Ce has a unique lanthanide element with 4f

[a]*School of Pharmaceutical & Chemical Technology, Zhenjiang College, Zhenjiang, 212028, PR China*

[b]*Jiangsu Higher Vocational College Engineering Research Center of Green Energy and Low Carbon Materials, Zhenjiang, 212028, PR China*

[c]*Jiangsu Key Laboratory of Advanced Catalytic Materials and Technology, School of Petrochemical Engineering, Changzhou University, Changzhou, 213164, China. E-mail: zdchen@cczu.edu.cn*

[d]*Qualtec Co., Ltd, Osaka, 590-0906, Japan*

† Electronic supplementary information (ESI) available. See DOI: https://doi.org/10.1039/d4ra08980d

electrons, variable valence states and coordination numbers. Its strong 3d–4f orbital electron coupling effect can cause electron disturbance and improve catalytic efficiency.[32,33] An effective way to improve on the low electrical conductivity situation is *in situ* growth of MOFs onto a conductive substrate though electrodeposition, which can considerably accelerate electron and mass transfer.[34–36]

Hybridization of MOF with external guest matrices to construct heterostructures can effectively modulate the atomic and electronic structures of heterogeneous catalysts and optimize the binding energy of intermediates, which helps to enhance OER performance.[37–39] In particular, iron oxyhydroxide (FeOOH) as an electrocatalyst has attracted widespread attention towards OER due to its natural abundance, open structure, and environmental friendliness.[40–42] However, the inferior electronic conductivity of FeOOH is a major factor that hinders its development. In fact, the most potential earth-abundant OER catalysts are FeNi or FeCo-based products. Recently studies demonstrated there are strong interactions between Fe and Ni or Co inducing excellent catalytic activity. The strong electron-capturing and hydrogen absorption ability of Co in FeOOH, which further promotes the formation and stabilization of FeOOH.[43,44]

Motived by above considerations, we produced an excellent electrically conductive Co–FeOOH/CoCe-MOF/NF substrate by a facile electrochemical deposition approach to construct of heterogeneous interfaces by *in situ* growth of Co–FeOOH nanosheets on CoCe-MOF. The resultant Co–FeOOH/CoCe-MOF/NF heterostructure is rich in strong coupling interfaces, which are benefit to provide more available active sites, strengthen the conductivity of the catalyst and accelerate the charge transfer kinetics, thus enhancing the catalytic activity. Based on these merits, Co–FeOOH/CoCe-MOF/NF heterostructure catalyst exhibits satisfactory OER and HER performance in alkaline solutions, only requiring low overpotentials of 226 and 74 mV at 10 mA cm^{-2}, respectively. Moreover, as-assembled Co–FeOOH/CoCe-MOF/NF‖Co–FeOOH/CoCe-MOF/NF can drive a water splitting current density of 10 mA cm^{-2} at an applied voltage of just 1.55 V in 1 M KOH. This work provides a reliable reference for constructing an efficient integrated MOFs-based bifunctional electrocatalyst to achieve water splitting.

2. Experimental

2.1. Synthesis of CoCe-MOF/NF thin film

Before electrodeposition, the nickel foam (NF, 1 cm × 1 cm, thickness: 1 nm) was cleaned with 1 M HCl, ethanol and deionized water by sonication for 15 min to remove the nickel oxides and oil stains. 44.2 mM of $Co(NO_3)_2 \cdot 6H_2O$ and 33.6 mM of $Ce(NO_3)_3 \cdot 6H_2O$ as the cation source, 5.6 mM of 2-NH_2-BDC as the organic ligand and 0.05 M of $NaNO_3$ as the supporting electrolyte were dissolved in the mixed solution of DMF and deionized water (50 : 50 vol%). Then, the solution was sonicated for 10 min and stirred for 30 min. Subsequently, the electrodeposition was carried out in the above prepared solution by applying a suitable potential (−1.4 V) for 500 s at room temperature, in which a standard three-electrode cell was used with a piece of NF, saturated calomel electrode (SCE) and platinum slice as working, reference, and counter electrodes, respectively. The CoCe-MOF/NF was obtained *via* washing with ultrapure three times and drying at 60 °C. To achieve an electrode with excellent electrocatalytic performance without formation of defects or detachment form the substrate surface, the electrodeposition time (100 s, 300 s, 500 s, 700 s and 900 s), reductive potential (−1.0 V, −1.2 V, −1.4 V, −1.6 V and −1.8 V), and the molar ratio of Co : Fe in the bath solution (4 : 1, 4 : 2, 4 : 3, 1 : 1, 3 : 4, 2 : 4 and 1 : 4) were all optimized.

2.2. Synthesis of Co–FeOOH/CoCe-MOF/NF thin film

The obtained CoCe-MOF/NF as the working electrode was immersed into a 20 mL aqueous solution containing 0.1 M $Co(NO_3)_2 \cdot 6H_2O$ and 0.1 M $Fe(NO_3)_3 \cdot 9H_2O$. An SCE as working reference electrode and platinum slice as a counter electrode were also immersed into this electrolyte solution. The constant potential was implemented at −1.2 V *vs.* SCE for 300 s to obtain the Co–FeOOH anchored the surface of CoCe-MOF/NF, which was named as Co–FeOOH/CoCe-MOF/NF.

2.3. Synthesis of RuO_2 and Pt/C electrode on NF

For comparison, 6 mg of RuO_2 or Pt/C powders were dispersed to the ethanol (100 μL) and Nafion (200 μL) mixture by ultrasonication for 30 min to form a homogeneous ink. Afterward, 50 μL of the ink was dropped on the treated NF surface. The samples were further dried to obtain the RuO_2/NF and Pt/C/NF.

2.4. Electrochemical measurements

Both of the OER and HER electrocatalytic performances were conducted on a CHI 660E electrochemical workstation (Shanghai Chenhua, China) in a typical three-electrode cell in 1 M KOH at room temperature. A carbon rod, a Hg/HgO electrode and the as-prepared samples served as the counter electrode, the reference electrode, and the working electrode (1 × 1 cm), respectively. Cyclic voltammetry (CV) was conducted with a scan rate of 50 mV s^{-1} to activate the electrode. Then, linear sweep voltammetry (LSV) curves were obtained at a scan rate of 2 mV s^{-1} from −0.115 to −0.785 V *vs.* RHE for HER, and from 0.915 to 1.915 V *vs.* RHE for OER in 1 M KOH, respectively. The measured potentials for OER *vs.* SCE were converted to the reversible hydrogen electrode (RHE) with the Nernst equation: $E_{RHE} = E_{SCE} + 0.242 + 0.0591 \times pH$, and the measured potentials for HER *vs.* SCE were converted to the RHE with the Nernst equation: $E_{RHE} = E_{SCE} + 0.197 + 0.0591 \times pH$. The double layer capacitance (DLC) was obtained by CV with scanning rates of 1 mV s^{-1}, 2 mV s^{-1}, 3 mV s^{-1}, 4 mV s^{-1}, 5 mV s^{-1} and 6 mV s^{-1}, respectively. Electrochemical impedance spectroscopy (EIS) was performed with the frequency range from 0.01 Hz to 100 000 Hz for HER, the initial potential of EIS is the open circuit voltage under performance conditions.

3. Results and discussion

3.1. Composites fabrication and characterization

The fabrication process of Co–FeOOH/CoCe-MOF/NF materials is depicted in Fig. 1. The CoCe-MOF is firstly grown on the NF *via* a electrodeposition method.

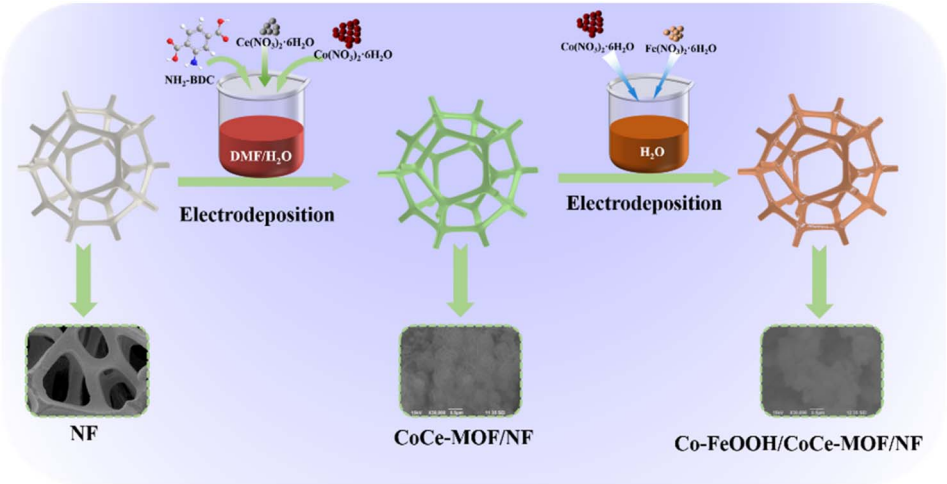

Fig. 1 Schematic illustration of the formation of 3D flower-like hollow NiCoFe LDH/NF nanostructure.

Afterward, Co–FeOOH is *in situ* grown on CoCe-MOF/NF to form the Co–FeOOH/CoCe-MOF/NF *via* electrodeposition progress.

The structure and morphology of a series of modified electrodes were first investigated by scanning electron microscopy (SEM) and Transmission electron microscopy (TEM). The SEM image clearly demonstrates the nanoparticle structure of Co–FeOOH/NF (Fig. 2A). As shown in Fig. 2B, the resultant CoCe-MOF/NF display a flower-like microsphere structure composed of abundant 2D nanosheets. The morphology of Co–FeOOH/CoCe-MOF/NF is studied by SEM and TEM (Fig. 2C and D), after deposition of Co–FeOOH, the CoCe-MOF/NF with many nanosphere particles evenly distributed on its surface. For the Co–FeOOH/CoCe-MOF/NF sample (Fig. 2E), the interlayer spacing of the CoCe-MOF/NF was approximately 0.22 nm, corresponding to the (111) plane, consistent with the X-ray diffraction (XRD) data. The corresponding element mapping results (Fig. 2F) elucidated the homogeneous distribution of Co, Ce and Fe elements on the surface of the Co–FeOOH/CoCe-MOF/NF sample, suggesting that the Co–FeOOH/NF is uniformly dispersed throughout the CoCe-MOF/NF surface.

In order to analyze the structure and composition of the samples, the X-ray diffraction (XRD) and Fourier transform infrared (FT-IR) spectra were carried out on Co–FeOOH/NF, CoCe-MOF/NF and Co–FeOOH/NF/CoCe-MOF/NF. As shown in Fig. 3A, there is no distinct peaks in the XRD spectra of Co–

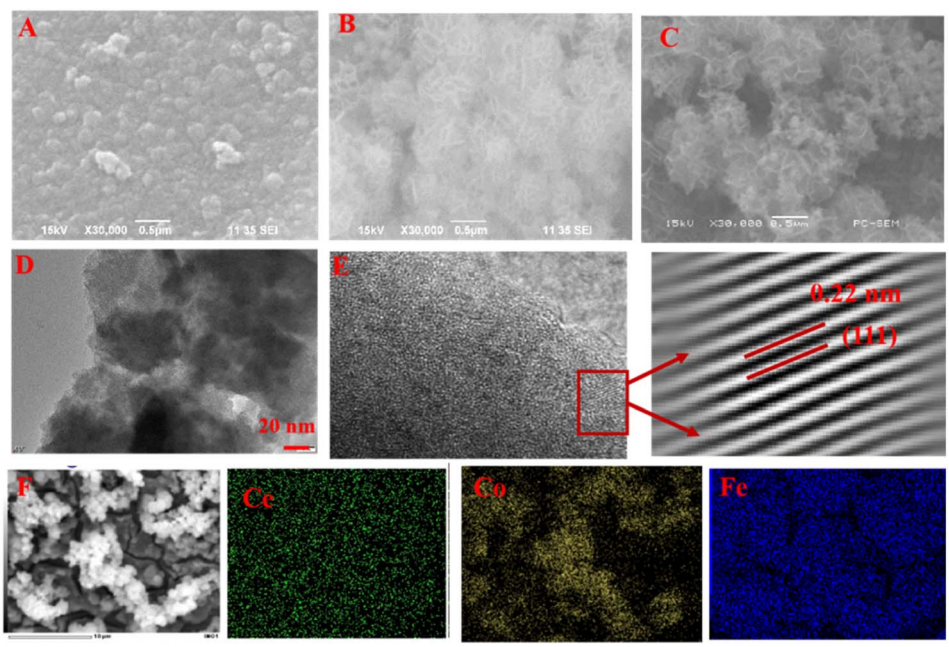

Fig. 2 SEM image of (A) Co–FeOOH/NF, (B) CoCe-MOF/NF, (C) SEM image, (D) TEM image, (E) HRTEM image and (F) elemental mapping of image of Co–FeOOH/CoCe-MOF/NF.

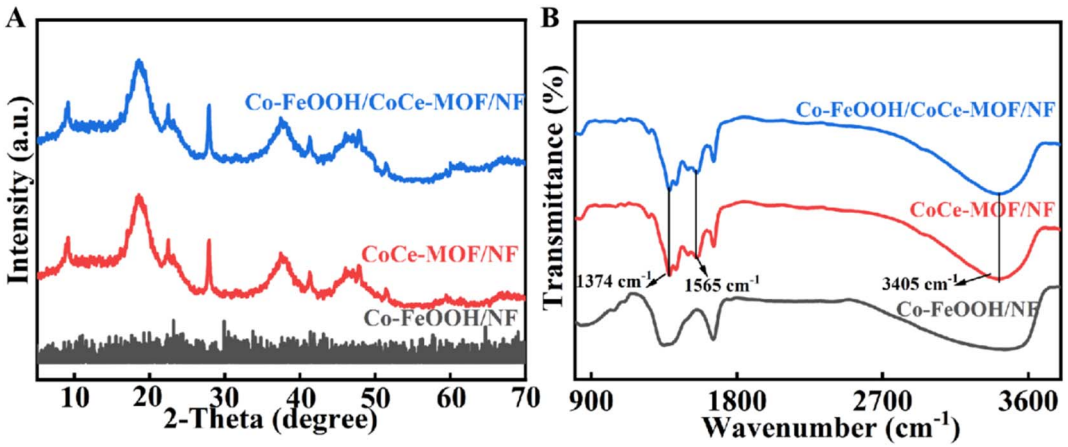

Fig. 3 XRD (A) and FT-IR (B) image of Co–FeOOH/NF, CoCe-MOF/NF and Co–FeOOH/CoCe-MOF/NF.

FeOOH/NF. In addition, the XRD peak of the obtained CoCe-MOF/NF samples are indexed to the related literature.[45] In the XRD patterns of Co–FeOOH/NF/CoCe-MOF/NF, the peaks are well matched with the pattern of CoCe-MOF/NF(JCPDS: 34-0394). These results reveal that the Co–FeOOH/NF may be amorphous, and it also shows that the deposition of Co–FeOOH does not affect the crystal structure of CoCe-MOF, which is consistent with the SEM and TEM results.

As shown in Fig. 3B, in the FT-IR of CoCe MOF/NF, the absorption peaks located at 1670 cm^{-1}, 1565 cm^{-1}, and 1374 cm^{-1} are N–H, C=N, and C–N bonds, respectively. The broad absorption band centered at 3405 cm^{-1} corresponds to the C=H bond, which once again proves the successful preparation of CoCe MOF/NF. In the FT-IR of Co FeOOH/NF, 1374 cm^{-1} and 1605 cm^{-1} correspond to O–H and M–O. In the FT-IR spectra of Co FeOOH/CoCe MOF/NF, peaks of CoCe MOF/NF and Co FeOOH/NF can be observed simultaneously, indicating the successful preparation of Co FeOOH/NF/CoCe MOF/NF.

X-ray photoelectron spectroscopy (XPS) measurements were carried out to elucidate the surface composition and elemental oxidation state of the Co–FeOOH/CoCe-MOF/NF electrode. The XPS survey spectra of Co–FeOOH/CoCe-MOF/NF composite exhibits Co 2p, Ce 3d, Fe 2p, C 1s, O 1s, and N 1s, demonstrating composites containing Co, Ce, Fe, C, O, and N components, as seen in Fig. 4A. For the high-resolution Ce 3d spectrum (Fig. 4B), the peaks denoted as v_1 (≈888.2 eV) and u_1 (≈904.2 eV) were attributed to the Ce $3d_{5/2}$ and Ce $3d_{3/2}$ of Ce^{3+}, respectively, while the peaks denoted as v (≈882.3 eV), v_2 (≈891.2 eV), v_3 (≈897.2 eV), u (≈901.9 eV), u_2 (≈912.2 eV), and u_3 (≈922.6 eV) corresponded to the Ce^{4+} species. The XPS spectrum of O 1s (Fig. 4C) is fitted to obtain three peaks near

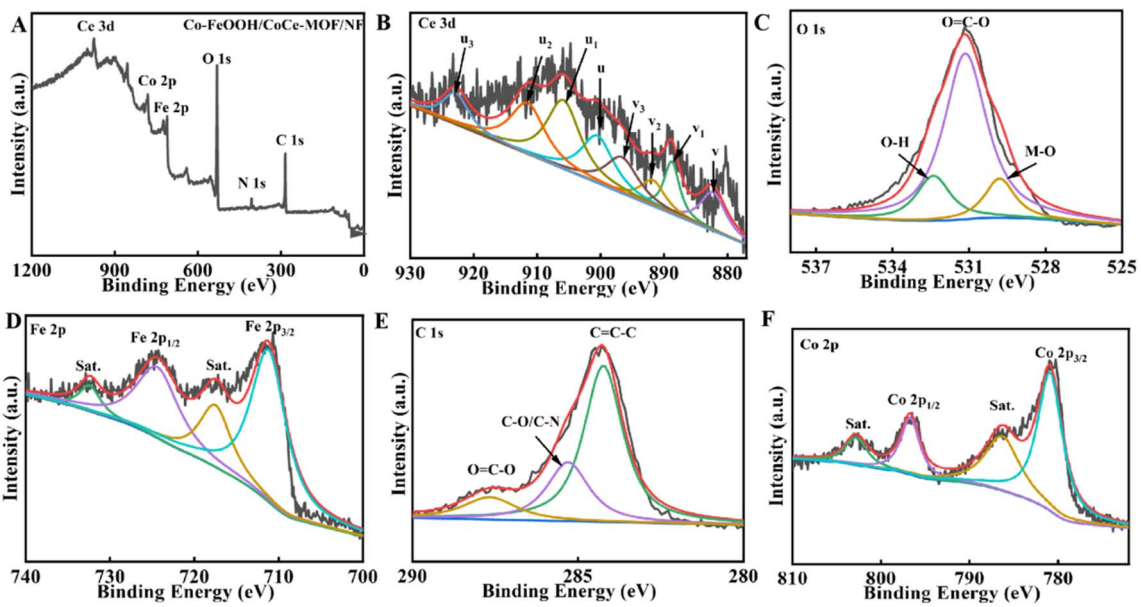

Fig. 4 XPS investigation of the Co–FeOOH/CoCe-MOF/NF sample: (A) survey spectrum, (B) Ce 3d, (C) O 1s, (D) Fe 2p, (E) C 1s and (F) Co 2p.

532.1 eV, 531.3 eV and 529.6 eV, representing O–H, O═C–O and M–O, respectively. This may be related to the formation of Fe–O and Co–O bonds, preliminarily proving the existence of Co–FeOOH. The Fe $2p_{1/2}$ and Fe $2p_{3/2}$ peaks at 725.2 and 712.1 eV confirm that the Fe element is mainly present as Fe(III) (Fig. 4D). The two satellite peaks at 730.4 and 717.2 eV further prove the +3 oxidation state for Fe. In the C 1s XPS spectra (Fig. 4E), the divided peaks at 284.2, 285.6, and 288.7 eV were assigned to C–C/C═C, C–O/C–N, and O–C═O, respectively. Similarly, the deconvoluted Co 2p spectrum (Fig. 4F) typically displays two characteristic peaks at 781.4 and 797.4 eV corresponding to Co $2p_{3/2}$ and Co $2p_{1/2}$ of a high-spin Co^{2+} state along with two distinct satellite peaks (787.3 and 803.1 eV). These results indicate that Co^{2+} on the surface of the Co–FeOOH/CoCe-MOF/NF catalyst.

3.2. Electrocatalytic performance for OER and HER

The electrochemical properties of the as-fabricated catalysts for OER were investigated in 1.0 M KOH. For comparison, the LSV curves of Ce-MOF/NF, Co-MOF/NF, CoCe-MOF/NF, Co–FeOOH/NF, Co–FeOOH/CoCe-MOF/NF and RuO_2/NF were also analyzed under the same condition. As displayed in Fig. 5A, the CoCe-MOF/NF requires the overpotentials of 256 mV at the current density of 10 mA cm^{-2}, which is less than that of the Ce-MOF/NF (380 mV) and Co-MOF/NF (310 mV). The improvement of electrocatalytic activity is due to the synergy between Co and Ce. Whereas after deposition of Co–FeOOH, the catalytic activity of Co–FeOOH/CoCe-MOF/NF is obviously improved and manifests the higher catalytic activity with a low overpotential of only 226 mV at 10 mA cm^{-2}, which is much lower than Co–FeOOH/NF (248 mV), CoCe-MOF/NF and commercial RuO_2/NF (259 mV) owing to the heterojunction effect between Co–FeOOH and CoCe-MOF components. Apparently, the electrochemical properties of the Co–FeOOH/CoCe-MOF/NF are comparable to those previously reported MOF-based catalysts (Table S1†). The overpotentials at 10 and 20 mA cm^{-2} were listed in Fig. 5B. The electrocatalytic reaction kinetics behavior is assessed by Tafel slopes of the corresponding catalyst, which are derived from linear fitting of LSV curve. As shown in Fig. 5C, the Co–FeOOH/CoCe-MOF/NF catalyst achieves the lowest Tafel slope of 54.8 mV dec^{-1} compared to those of other catalysts (167.1 mV dec^{-1} for Ce-MOF/NF, 123.6 mV dec^{-1} for Co-MOF/NF, 65.8 mV dec^{-1} for CoCe-MOF/NF, 56.8 mV dec^{-1} for Co–FeOOH/NF, and 75.1 mV dec^{-1} for RuO_2/NF), thus proving its faster OER kinetic. The electrochemical impedance spectrum (EIS) energetic arc after the equivalent circuit diagram fit is illustrated in Fig. 5D, in which the arc radius of Co–FeOOH/CoCe-MOF/NF was observed to be smaller than those of the Co–FeOOH/NF and CoCe-MOF/NF catalyst. This suggested that the deposition of Co–FeOOH significantly optimized the charge transfer and electron conductivity. Besides, good catalytic-activity, the durability of the catalysts is important for commercializing it into various energy conversion and storage technologies. Fig. 5E shows the multi-step chronopotentiometric curve of the Co–FeOOH/CoCe-MOF/NF. At 50 mA cm^{-2}, the corresponding potential immediately responds to the current density and remains stable for 300 s and the potential change is very negligible in every current density. The long-term stability of the Co–FeOOH/CoCe-MOF/NF catalyst was also tested by chronopotentiometry (CP) measurements (Fig. 5F). The Co–FeOOH/CoCe-MOF/NF catalyst could retains its constant overpotential for 16 h at a set current density of 10 mA cm^{-2} and voltage increase after 3000 cycles going from 1.48 V (black curve) to 1.5 V (red curve) at the current density of 20 mA cm^{-2}. These results all confirming its excellent stability and durability.

To get a deep insight into the intrinsic activity of electrocatalysts, the CV curves with different scanning rates are

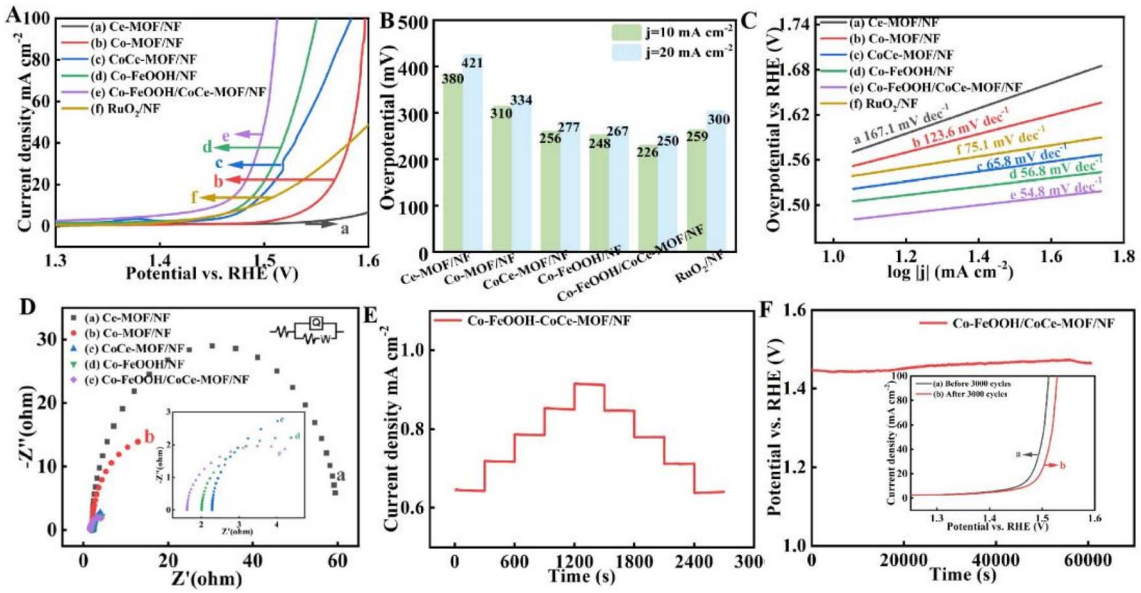

Fig. 5 Electrocatalytic performance evaluation for OER. (A) LSV curve. (B) Comparison of overpotential at 10 and 20 mA cm^{-2}. (C) Tafel plots. (D) EIS spectra. (E) Multistep chronopotentiometry at different current densities. (F) Chronopotentiometry curves at 10 mA cm^{-2}.

measured to investigate the C_{dl} of the materials, which is proportional to electrochemically active surface areas (Fig. S1†). The most active Co–FeOOH/CoCe-MOF/NF exhibits the highest C_{dl} value of 0.57 mF cm^{-2} (Fig. S2†), suggesting its largest electrochemical active surface area with more active sites. To further explore the changes in crystal structure and micromorphology of the catalyst after chemical reaction, we characterize the electrode after OER process. As shown in Fig. S3,† the major peaks of Ce 3d shifted to lower binding energies after OER stability tests. Specifically, the two spin–orbit splitting peaks of Ce $3d_{1/2}$ and Ce $3d_{3/2}$ were shifted down by 1.26 eV and 1.55 eV after deconvolution, respectively, while the corresponding satellite peaks were also shifted. Notably, the difference in position between the Ce 3d spin–orbit splitting peaks after OER testing was 12.83 eV, which, along with the peak pattern, confirmed the presence of $Ni(OH)_2$.

The HER performances of all the as-prepared samples are estimated *via* LSV measurements in 1.0 M KOH at a scan rate of 2 mV s^{-1} (Fig. 6A). Co–FeOOH/CoCe-MOF/NF shows the best HER activity among all the samples, with low overpotentials of 74 mV to achieve HER current densities of 10 mA cm^{-2}, and is comparable to the benchmark Pt/C catalyst on the same NF substrate (72 for 10 mA cm^{-2}), which can be attributed to that the strong synergistic effects can expose abundant active sites, and the heterogeneous interfacial interactions between Co–FeOOH and CoCe-MOF/NF are conducive to enhance the intrinsic activity by optimizing the adsorption/desorption energy of intermediates in the catalytic reaction. On the other hand, the overpotentials are 143 mV (j_{10}) on Co–FeOOH/NF, 163 mV (j_{10}) on CoCe-MOF/NF, 182 mV(j_{10}) on Co-MOF/NF and 191 mV (j_{10}) on Ce-MOF/NF (Fig. 6B). Even better, the HER catalytic activity of Co–FeOOH/CoCe-MOF/NF outperforms many previously reported MOF-based electrocatalysts (Table S2†). The Tafel slope of Co–FeOOH/CoCe-MOF/NF is 70.1 mV dec^{-1}, which is comparable to that of Pt/C/NF (58.2 mV dec^{-1}) and much lower than that of Co–FeOOH/NF (73.4 mV dec^{-1}), CoCe-MOF/NF (120.3 mV dec^{-1}), Co-MOF/NF (128.3 mV dec^{-1}) and Ce-MOF/NF (276.5 mV dec^{-1}) (Fig. 6C), indicating significantly enhanced HER kinetics as well as improved water adsorption and dissociation efficiency owing to the interface microenvironment regulation of Co–FeOOH. Furthermore, EIS analysis is conducted to evaluate the charge transfer abilities of catalysts. From Fig. 6D, the Co–FeOOH/CoCe-MOF/NF shows the smallest charge transfer resistance (R_{ct}) estimated by the radius of the semicircles. In general, the smaller radius corresponds to the faster electron transfer rate on the surface of the electrode. As illustrated in Fig. 6E, when the Co–FeOOH/CoCe-MOF/NF was operated at different static voltages, the current densities remain almost unchanged at 50 mA cm^{-2} to 250 mA cm^{-2}. The durability of Co–FeOOH/CoCe-MOF/NF sample was assessed through the chronoamperometric test at onset potential for HER electrolysis over 16 h. As revealed in Fig. 6F, the current *vs.* time (*i–t*) chronoamperometric response exhibits a very slow attenuation with high current retention after 16 h. And continuous 3000 CV scanning between 0.1 V and −0.3 V (*vs.* RHE) leads to almost no degradation in current density, confirming its excellent stability and durability.

3.3. Overall water splitting performance

The overall alkaline water splitting on bifunctional Co–FeOOH/CoCe-MOF/NF as anode and cathode (Co–FeOOH/CoCe-MOF/NF‖Co–FeOOH/CoCe-MOF/NF) was evaluated on a two-electrode system in 1.0 M KOH. Obviously, the Co–FeOOH/CoCe-MOF/NF(+)‖Co–FeOOH/CoCe-MOF/NF(−) couple exhibits excellent overall water splitting performance. As shown in Fig. 7A, in 1 M KOH, this electrolyzer can achieve current densities of 10 mA cm^{-2} at cell voltages of 1.55 V, which is

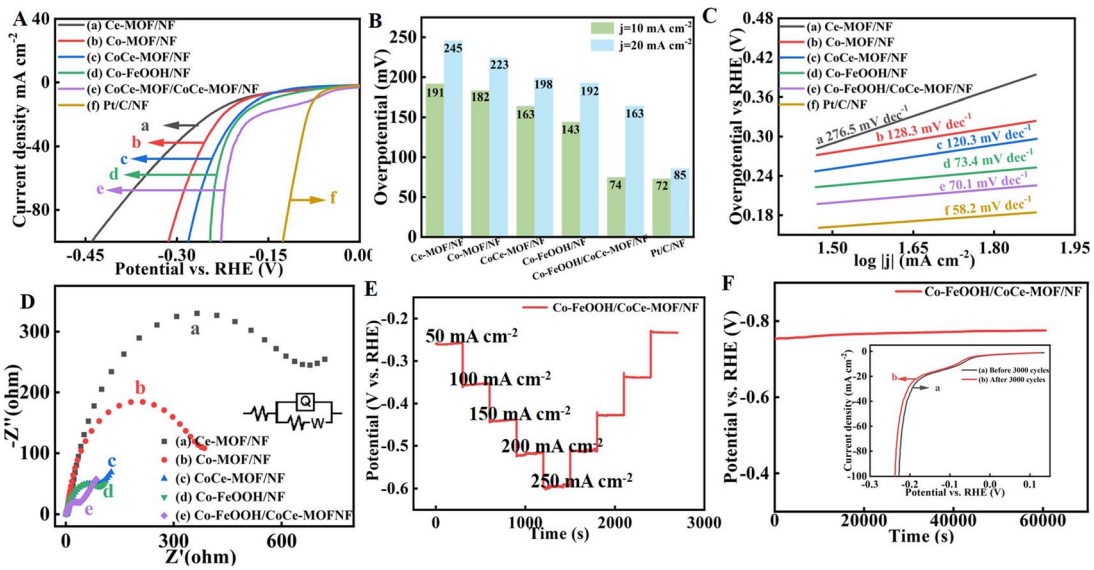

Fig. 6 Electrocatalytic performance evaluation for HER. (A) LSV curve. (B) Comparison of overpotential at 10 and 50 mA cm^{-2}. (C) Tafel plots. (D) EIS spectra. (E) Chronopotentiometry curves at 10 mA cm^{-2}. (F) Multistep chronopotentiometry at different current densities.

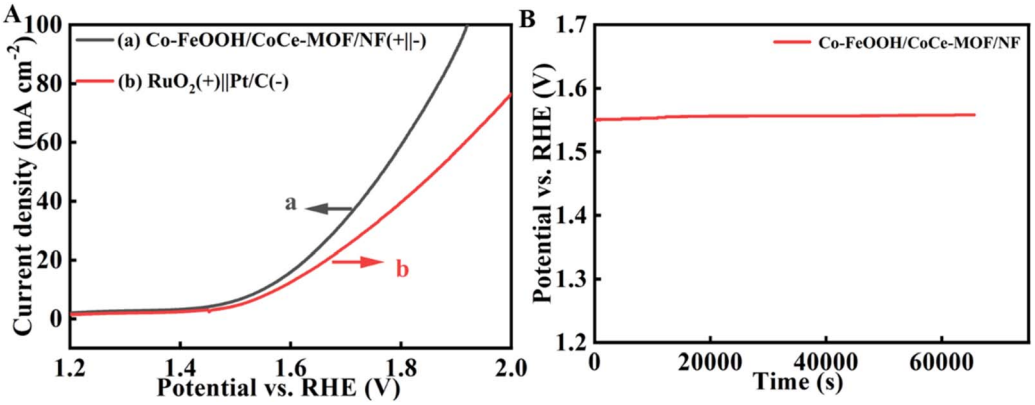

Fig. 7 (A) Comparison in 1 M KOH for various electrocatalysts. (B) Stability testing of Co–FeOOH/CoCe-MOF/NF catalyst for overall water splitting performance conducted in 1 M KOH.

significantly better than noble metal catalysts (RuO_2/NF(+)||Pt/C/NF(−), 1.63 V at 10 mA cm^{-2}), as well as the vast majority of other MOF-based electrocatalytics (Table S3†). Tests were conducted to evaluate the reaction stability when electrocatalysis was carried out by Co–FeOOH/CoCe-MOF/NF(+)||Co–FeOOH/CoCe-MOF/NF(−), with results listed in Fig. 7B.

4. Conclusion

In summary, an effective combination of Co–FeOOH and CoCe-MOF enables the Co–FeOOH/CoCe-MOF/NF with excellent OER performance as low overpotential of 226 mV at 10 mA cm^{-2} and small Tafel slopes of 54.8 mV dec^{-1} and outstanding HER performance as low overpotential of 70.1 mV at 10 mA cm^{-2} and small Tafel slopes of 73.6 mV dec^{-1}. Encouraged by high OER and HER activity, the optimal Co–FeOOH/CoCe-MOF/NF(+)||Co–FeOOH/CoCe-MOF/NF(−) couple delivers only 1.55 V at 10 mA cm^{-2} with robust stability, which is superior to most of previously reported bifunctional MOF-based catalysts. The excellent catalytic activity on bifunctional Co–FeOOH/CoCe-MOF/NF should be attributed to following reasons: (1) the 3D flower structure of CoCe-MOF effectively increase the specific surface area and expose more active sites, and dense hole array can provide faster mass transport and shorter ion diffusion length; (2) the mixing of crystalline and amorphous structures at the nanoscale to form heterogeneous structures and interfaces is particularly crucial as it significantly enhances the activity and stability of catalysts. The findings in this work offer an in-depth understanding as well as important guidance for further development of high-performance heterojunction structure.

Author contributions

Chang Su: writing – original draft; methodology; data curation; conceptualization. Dan Wang: software; investigation. Wenchang Wang: supervision; visualization. Naotoshi Mitsuzaki: formal analysis; project administration. Zhidong Chen: writing – review & editing; funding acquisition.

Conflicts of interest

There are no conflicts to declare.

Acknowledgements

This work was supported by the University level scientific research project of Zhenjiang College (key projects).

References

1 Y. Yu, Q. Chen, J. Li, P. Rao, R. Li, Y. Du, C. Jia, W. Huang, J. Luo, P. Deng, Y. Shen and X. Tian, *J. Colloid Interface Sci.*, 2022, **607**, 1091–1102.
2 J.-L. Liu, Y. Huang and J.-J. Wang, *J. Colloid Interface Sci.*, 2022, **617**, 525–532.
3 B. Singh, A. Yadav and A. Indra, *J. Mater. Chem. A*, 2022, **10**, 3843–3868.
4 B. Singh, *Dalton Trans.*, 2024, **53**, 15390–15402.
5 H. Yang, Z. Zhou, H. Yu, H. Wen, R. Yang, S. Peng, M. Sun and L. Yu, *J. Colloid Interface Sci.*, 2023, **636**, 11–20.
6 W. Li, Y. Deng, L. Luo, Y. Du, X. Cheng and Q. Wu, *J. Colloid Interface Sci.*, 2023, **639**, 416–423.
7 T. Wang, X. Liao, T. Zhang, M. Dai and H. Lin, *Composites, Part B*, 2023, **254**, 110601.
8 X. Chen, D. Li, Y. Li, W. Zhan, C. Huang, R. Chen, W. Wang, H. Ni and P. K. Chu, *Appl. Surf. Sci.*, 2022, **574**, 151636.
9 R. Deng, M. Guo, C. Wang and Q. Zhang, *Nano Mater. Sci.*, 2022, **6**(2), 139–173.
10 B. Singh, N. Verma, P. Arora and A. Draksharapu, *ACS Appl. Nano Mater.*, 2024, **7**, 27064–27070.
11 M. Sohail, M. Ayyob, A. Wang, Z. Sun, A. Syed, A. M. Elgorban, A. H. Bahkali, R. Zairov and I. Ahmad, *Int. J. Hydrogen Energy*, 2024, **67**, 1000–1008.
12 Y. Yao, J. He, L. Ma, J. Wang, L. Peng, X. Zhu, K. Li and M. Qu, *J. Colloid Interface Sci.*, 2022, **616**, 287–297.
13 M. Zhang, X. Ma, H. Zhong, J. Yang and Z. Cao, *J. Alloys Compd.*, 2023, **935**, 168135.

14 N. Chen, X. Du and X. Zhang, *Renewable Energy*, 2022, **193**, 715–724.
15 L. Mu, J. He, Y. Yao, J. Li, Q. Liu, Y. Xue, Y. Zhao, H. Liu and M. Qu, *Sep. Purif. Technol.*, 2024, **331**, 125717.
16 H. jinHuang, L. Xu, D. Yoon Woo, S. Kim, S. Min Kim, Y. Kyeong Kim, J. Byeon and J. Lee, *Chem. Eng. J.*, 2023, **451**, 138939.
17 B. Zhu, D. Xia and R. Zou, *Coord. Chem. Rev.*, 2018, **376**, 430–448.
18 F. Zheng, Z. Zhang, D. Xiang, P. Li, C. Du, Z. Zhuang, X. Li and W. Chen, *J. Colloid Interface Sci.*, 2019, **555**, 541–547.
19 Y. Zhou, R. Abazari, J. Chen, M. Tahir, A. Kumar, R. R. Ikreedeegh, E. Rani, H. Singh and A. M. Kirillov, *Coord. Chem. Rev.*, 2022, **451**, 214264.
20 B. Singh, R. Kumar and A. Draksharapu, *ACS Appl. Nano Mater.*, 2024, **7**, 15763–15771.
21 B. Singh and H. Gupta, *Chem. Commun.*, 2024, **60**, 8020–8038.
22 J. Li, T. Tan, Y. Xie, J. Chu, L. Li, B. Ouyang, E. Kan and W. Zhang, *J. Colloid Interface Sci.*, 2023, **640**, 78–90.
23 L. Ma, Q. Xue, Y. Dang, L. Wang and Y. Zhou, *J. Colloid Interface Sci.*, 2024, **655**, 234–242.
24 M. I. Anwar, T. Wang, M. Asad, K. Jabbour, S. Manzoor, L. Ma, N. Ahmed, W. Zhang, M. N. Ashiq and G. Yang, *Int. J. Hydrogen Energy*, 2024, **51**, 242–255.
25 B. Singh, R. Kumar and A. Draksharapu, *Coord. Chem. Rev.*, 2024, **7**(13), 15763–15771.
26 B. Cui, C. Wang, S. Huang, L. He, S. Zhang, Z. Zhang and M. Du, *J. Colloid Interface Sci.*, 2020, **578**, 10–23.
27 S. Xie, F. Li, S. Xu, J. Li and W. Zeng, *Chin. J. Catal.*, 2019, **40**, 1205–1211.
28 H.-W. Lin, D. Senthil Raja, X.-F. Chuah, C.-T. Hsieh, Y.-A. Chen and S.-Y. Lu, *Appl. Catal., B*, 2019, **258**, 118023.
29 L. Han, J. Xu, Y. Huang, W. Dong and X. Jia, *Chin. Chem. Lett.*, 2021, **32**, 2263–2268.
30 Q. Liu, J. Chen, P. Yang, F. Yu, Z. Liu and B. Peng, *Int. J. Hydrogen Energy*, 2021, **46**, 416–424.
31 J. Cai, Z. Xu, X. Tang, H. Liu, X. Zhang, H. Li, J. Wang and S. Li, *J. Alloys Compd.*, 2023, **947**, 169498.
32 Y. Liao, Y. Xiao, Z. Li, X. Zhou, J. Liu, F. Guo, J. Li and Y. Li, *Small*, 2023, **20**(12), 2307685.
33 J. Yu, X. Du, H. Liu, C. Qiu, R. Yu, S. Li, J. Ren and S. Yang, *Energy Fuels*, 2021, **35**, 19000–19011.
34 J. Wang, Y. Jiang, C. Liu, Y. Wu, B. Liu, W. Jiang, H. Li and G. Che, *J. Colloid Interface Sci.*, 2022, **614**, 532–537.
35 J. Li, W. Huang, M. Wang, S. Xi, J. Meng, K. Zhao, J. Jin, W. Xu, Z. Wang, X. Liu, Q. Chen, L. Xu, X. Liao, Y. Jiang, K. A. Owusu, B. Jiang, C. Chen, D. Fan, L. Zhou and L. Mai, *ACS Energy Lett.*, 2018, **4**, 285–292.
36 B. Singh, A. Singh, A. Yadav and A. Indra, *Coord. Chem. Rev.*, 2021, **447**, 214144.
37 M. Zhao, Y. Wang, W. Mi, J. Wu, J.-J. Zou, X.-D. Zhu, J. Gao and Y.-C. Zhang, *Electrochim. Acta*, 2023, **458**, 142513.
38 J. X. Feng, H. Xu, Y. T. Dong, S. H. Ye, Y. X. Tong and G. R. Li, *Angew. Chem., Int. Ed.*, 2016, **55**, 3694–3698.
39 D. Han, L. Hao, Y. Wang, Y. Gao, J. Yan and Y. Zhang, *J. Colloid Interface Sci.*, 2023, **652**, 1148–1155.
40 S. Kulandaivalu, L. K. Putri and A. R. Mohamed, *Int. J. Hydrogen Energy*, 2023, **48**, 26133–26147.
41 R. Li, Y. Wang, B. Chen, H. Zhang, C. Yan, X. Xu, M. Humayun, D. P. Debecker and C. Wang, *Int. J. Hydrogen Energy*, 2024, **51**, 1292–1302.
42 Z. Xu, Y. Jiang, J.-L. Chen and R. Y.-Y. Lin, *ACS Appl. Mater. Interfaces*, 2023, **15**, 16702–16713.
43 Y. Gu, X. Wang, M. Humayun, L. Li, H. Sun, X. Xu, X. Xue, A. Habibi-Yangjeh, K. Temst and C. Wang, *Chin. J. Catal.*, 2022, **43**, 839–850.
44 J. Liu, Y. Shi, Y. Gu, Z. Lv, L. Zhao, Y. Yang, T. Zhan, J. Lai and L. Wang, *Nano Res.*, 2023, **17**, 3675–3683.
45 M. Wang, F. Li, J. Dong, X. Lin, X. Liu, D. Wang and W. Cai, *J. Environ. Chem. Eng.*, 2022, **10**, 107892.